

AIAA'88

AIAA-88-0414

**Validation of a Multigrid Method
for the Reynolds Averaged Equations**

L. Martinelli, A. Jameson

Princeton University, Princeton N. J.

AIAA 26th Aerospace Sciences Meeting

January 11-14, 1988/Reno, Nevada

VALIDATION OF A MULTIGRID METHOD FOR
THE REYNOLDS AVERAGED EQUATIONS

Luigi Martinelli and Antony Jameson
Department of Mechanical and Aerospace Engineering
Princeton University
Princeton, New Jersey

Abstract

This paper describes recent improvements to a multigrid method for the solution of the compressible viscous conservation laws. The discretization scheme and the numerical algorithm are applied to the solution of the Reynolds' averaged equations with a simple algebraic closure. A validation study is carried out and the characteristics of the scheme are assessed by the calculation of several test cases. The effects of substituting an alternative formulation of the upwind biasing terms are also studied, and results obtained by using a flux limited dissipation model are presented.

The accuracy of the discretization scheme and the efficiency of the multigrid algorithm is demonstrated by comparison of the computed results with the solutions obtained by other numerical schemes and with available experimental data.

1. Introduction

The continuing evolution of supercomputers has moved the optimal trade off between cost and feasibility of computations and completeness of the mathematical model toward the solution of the full set of non linear conservation laws. However, even with the new generation of computers the resolution and the accuracy attainable in the solution of the Navier Stokes equations are still severely limited by the disparate length scales in the viscous region and the external flow. At high Reynolds numbers the problem is complicated further by the onset and development of turbulence. While there is the possibility of attacking the Navier Stokes equations for laminar flow problems, the solution of the complete set of equations for Reynolds numbers of practical interest in aeronautics still remains beyond the reach of currently available computers and any computer in the foreseeable future [1]. The problem of describing turbulent flows must still be approached by the solution of the Reynolds averaged equations that require a suitable turbulence model for closure. While the development of a fairly general and reliable turbulence model is still an open problem and represents a research effort by itself, improvements in the speed and accuracy of numerical schemes are still needed before complete viscous computations can be routinely performed. This work outlines the development of an accurate and efficient explicit multigrid scheme for the solution of 2-D viscous flow problems in aerodynamics [2]. Besides the fact that the analysis of 2-D configurations is of

practical interest in the early stages of a design, a systematic study of the accuracy of numerical methods in 3-D is severely limited by the memory of currently available computers. Nevertheless the numerical scheme of the present study can be generally carried over to the full 3-D viscous conservation laws.

The principal requirement for a satisfactory solution of viscous equations of gasdynamics is the reduction of the discretization error to a level such that any numerical dissipative phenomena, introduced by the scheme, should not interfere with the effects of physical transport phenomena. This problem is particularly severe in regions of strong interaction where, depending on the scale of the problem (the Reynolds number), an accurate solution is still impeded by the lack of powerful enough computers. A major source of difficulty in producing an adequate numerical simulation of a turbulent flow field about an airfoil is the need to use a mesh with a very fine grid spacing in the boundary layer and wake regions. Meshes of this type generally are highly stretched and contain cells with a very large aspect ratio. As the aspect ratio is increased the discretization schemes are known to suffer both loss of accuracy and a reduction in their convergence rate. These difficulties can be remedied by a careful control of discretization errors (e.g. artificial dissipation) and by improvements in the iteration schemes.

In the approach followed in the present study the discretization of the spatial operators is entirely separated from the time marching scheme. The conservation equations are first discretized by a finite volume technique using a cell centered formulation. A multistage scheme is then used to perform the integration to a steady state and to drive the solution on multiple grids [3,4,5]. A novel five stage scheme with three evaluations of the diffusion operator is proposed. It has the desirable property of an extended stability region along the negative real axis. The effects of artificial dissipation are also studied and results using two different models of upwind biasing are presented. These include the adaptive coefficient model of Jameson [3], and a flux limited dissipation model [6]. For steady state computations, efficiency of the iteration scheme is enhanced by the use of multiple grids, and locally varying time steps. A novel implicit smoothing technique with locally varying smoothing coefficients is also proposed to accelerate convergence to a steady state. In the next sections the principal features of the numerical scheme are reviewed and an evaluation of the accuracy and speed of the algorithm is carried out by computing some of the test cases

of the 1987 Viscous Transonic Workshop [7] for three different wing sections.

2. Mathematical Model

Following Rubesin and Rose [8], the density ρ , the pressure p , the shear stress tensor σ_{ij} , and the components of the heat flux vector q_i are decomposed in a time averaged mean (\bar{g}), and a fluctuation ($g' = g - \bar{g}$). The velocity components u_i , the internal energy per unit mass e , the molecular viscosity coefficient μ , and the thermal conductivity k are decomposed into a mass-weighted averaged (\bar{g}) and a local instantaneous fluctuation ($g'' = g - \bar{g}$). When the expansion of the dependent variables is carried out in the differential conservation laws and a time average of the equations is taken, the following equations are obtained:

$$\frac{\partial \bar{p}}{\partial t} + \frac{\partial}{\partial x_j} (\bar{\rho} \tilde{u}_j) = 0 \quad (2.1)$$

$$\frac{\partial \bar{\rho} \tilde{u}_i}{\partial t} + \frac{\partial}{\partial x_j} \left[\bar{\rho} \tilde{u}_j \tilde{u}_i + \bar{p} \delta_{ij} - (\bar{\sigma}_{ij} - \overline{\rho u''_i u''_j}) \right] = 0 \quad (2.2)$$

$$\begin{aligned} \frac{\partial \bar{\rho} \tilde{E}}{\partial t} + \frac{\partial}{\partial x_j} \left[\bar{\rho} \tilde{u}_j \tilde{E} - \tilde{u}_i (-\bar{p} \delta_{ij} + \bar{\sigma}_{ij} - \overline{\rho u''_i u''_j}) - \right. \\ \left. \overline{u''_i (-\bar{p} \delta_{ij} + \bar{\sigma}_{ij} - 1/2 \rho u''_i u''_j)} + \right. \\ \left. \bar{q}_j + \overline{\rho u''_j e''} \right] = 0 \end{aligned} \quad (2.3)$$

Because of the Reynolds decomposition and averaging, extra terms (the correlation tensors) arise in the equations. Physically those terms represent the turbulent transport of momentum and energy due to velocity and pressure fluctuations. The mean energy dissipation

$\overline{u''_i (p \delta_{ij} + \sigma_{ij} - 1/2 \rho u''_i u''_j)}$ is generally neglected on the basis of an order of magnitude consideration. One can also observe that by defining

$$\sigma_{ij \text{ tot}} = \bar{\sigma}_{ij} - \overline{\rho u''_i u''_j} \quad (2.4)$$

$$q_{j \text{ tot}} = \bar{q}_j + \overline{\rho u''_j e''} \quad (2.5)$$

the equations are reduced to the same form as the instantaneous Navier Stokes equations.

In the present study the Reynolds stress tensor is modeled as being proportional to the rate of deformation tensor of the mean flow. Therefore the expression for the total stress tensor is assumed to be:

$$(\sigma_{ij})_{\text{tot}} = \mu_{\text{tot}} (\nabla u + \nabla u^T - \frac{2}{3} \nabla \cdot u \delta_{ij}) \quad (2.6)$$

where $\mu_{\text{tot}} = \mu_{\text{lam}} + \mu_{\text{turb}}$, and μ_{turb} is the eddy viscosity coefficient. Similarly, the total heat flux vector results:

$$q = -\gamma \left[\frac{\mu_{\text{lam}}}{Pr} + \frac{\mu_{\text{turb}}}{Pr_{\text{turb}}} \right] \nabla \tilde{e} \quad (2.7)$$

The eddy viscosity is computed by using a simple algebraic turbulence model [9].

3. Numerical Discretization

The unknown vector w is stored at the center of the computational cell and the approximation of the convective operator is obtained as follows [3]. First the flux velocity Q_l is evaluated on each side of the l -th edge as:

$$Q_l^+ = \frac{\Delta y (\rho u)_l^+ - \Delta x (\rho v)_l^+}{\rho_l^+} \quad (3.1)$$

$$Q_l^- = \frac{\Delta y (\rho u)_l^- - \Delta x (\rho v)_l^-}{\rho_l^-}$$

where Δy and Δx are the increments of x and y along the l -th edge with the appropriate sign. Then the net flux across the l -th edge can be evaluated as

$$F_l = \frac{1}{2} (Q_l^+ w^+ + Q_l^- w^-) \quad (3.2)$$

Finally the net contribution of convection to the balance in the ij cell is computed as

$$C(w)_{ij} = \sum_{l=1}^4 F_l \quad (3.3)$$

This discretization reduces to central differencing on a cartesian grid and is second order accurate on a mesh with a smooth variation in the cell distribution.

In constructing an approximation to the viscous terms, we wish to retain all the advantages of the finite volume formulation which are a consequence of its derivation from the integral form of the equations [5]. Thus a similar flux balance is formed for the viscous terms also using the cell as a control volume. The numerical estimate of the viscous terms, however, needs an approximation of the first partial derivatives of the velocity and temperature to evaluate the shear stress and heat flux components. For computing these derivatives we make use of a discrete form of the Gauss theorem, which is applied on the path joining the centers of two adjacent cells with the end points of their dividing side. This requires averaging of the flow variables at the cell vertices but gives an estimate of the derivatives directly at the mid-point of the edges [5]. For the l -th edge we have:

$$\phi_l = (f_{vl} \Delta y - g_{vl} \Delta x) \quad (3.4)$$

where f_{vl} , g_{vl} are the viscous fluxes.

The net viscous flux contribution out of the computational cell is then obtained by summing over the four sides as:

$$D(w)_{ij} = \sum_{l=1}^4 \phi_l \quad (3.5)$$

The discretization procedure developed here is easily extended to treat additional field equations required by differential turbulence models. If an algebraic model is used, however, it is more convenient to compute the eddy viscosity at the center of the computational cell.

4. Artificial Dissipation

The finite volume scheme is intrinsically dissipative in regions where the physical viscous terms dominate. However, moving away from the solid boundaries and the wake regions, the convective operator starts to play a major role. This is partly due to the fact that the physical effects of transport die out, and it is partly caused by the stretching of the computational mesh that contributes to a loss of resolution in the approximation of the viscous terms. In both cases the possibility of undamped oscillatory modes common to the treatment of the Euler equations arises. Therefore in order to avoid decoupling of even and odd points the addition of artificial dissipative terms is needed. A second reason for introducing additional dissipative terms is to allow the clean capture of shock waves. The Navier Stokes equations should give in principle an accurate description of the structure of a weak shock wave. However, the thickness of the shock which is of the order of the mean free path, is so small that its resolution would require an extremely fine mesh that cannot be attained even with the new generation of computers. For this reason it pays off to trade some of the accuracy in the neighborhood of the shock wave in favor of damping undesirable oscillations.

It is known that shock waves can be effectively captured with a simple formulation by introducing a low background level of dissipation that is increased in the neighborhood of the shock wave to a peak value proportional to the local wave speed. In this model the dissipative terms are constructed in a similar manner for every equation by using a flux balance formulation that preserves the original conservation form, and the level of the artificial dissipation introduced is controlled by making use of adaptive coefficients. The use of such a dissipation model has been proved successful in computing accurate inviscid solutions on highly stretched meshes and in calculations of laminar flow problems [5]. Besides its simplicity, this formulation is particularly attractive for viscous calculations since it allows the precise monitoring of the magnitude of the artificial dissipation terms and

their relative weight with respect to the physical terms.

The use of an alternative upwind biasing technique is also investigated in the present study. This second formulation makes use of flux difference splitting in conjunction with flux limited dissipation [6]. The flux difference splitting technique offers an avenue for extending the construction of total variation diminishing (TVD) schemes to treat a system of conservation laws by separating the characteristic fields corresponding to the different wave speeds.

Following Roe [10], a linear mapping

$$A(w_{i+1}, w_i)$$

with the property that

$$A(w_{i+1}, w_i) \times (w_{i+1} - w_i) = f(w_{i+1}) - f(w_i)$$

is introduced and expressed in terms of a diagonal matrix Λ containing its eigenvalues:

$$A = T \Lambda T^{-1}$$

The dissipative fluxes are then constructed from third differences of the characteristic variable $T^{-1}w$ [6], namely

$$d_{i+1/2} = -\phi_{i+1} e_{i+3/2} + 2e_{i+1/2} - \phi_i e_{i-1/2}$$

where:

$$e_{i+1/2} = \Lambda_{i+1/2} \{ (T^{-1}w)_{i+1} - (T^{-1}w)_i \}$$

and ϕ is a limiter for the antidiffusive fluxes.

5. Integration Scheme

An hybrid multistage scheme [3] is used for integrating the time dependent equations to a steady state and to drive the multigrid cycle. The optimal choice of the integration scheme depends on a trade-off between the extent of the stability region and the cost of the integration. A very effective five stage scheme with coefficients,

$$a_1 = \frac{1}{4}, \quad a_2 = \frac{1}{6}, \quad a_3 = \frac{3}{8}, \quad a_4 = \frac{1}{2}$$

and three evaluations of the dissipative operators at the first, third, and fifth stage is proposed. The stability region of this scheme, obtained by Fourier analysis of the linear one-dimensional model problem [3]

$$u_t + u_x + \mu \Delta x^3 u_{xxxx} = 0,$$

is shown in fig. (5.1). If a multistage scheme is used to solve such a model problem, the amplification factor $f(z)$ can be recursively computed as a function of the Fourier symbol of the residual

$$z = -i\lambda \sin\{-4\lambda\mu(1-\cos\zeta)\}^2,$$

where $\lambda = \Delta t/\Delta x$ is the CFL number. The stability region is then given in the complex z -plane by

those values of z for which $|f(z)| < 1$. The stability region of this scheme extends to a value of the CFL of 4 along the imaginary axis and about 9 along the real axis (fig. 5.1). This particular scheme also exhibits good high frequency damping characteristics and therefore is appropriate to drive the multigrid algorithm.

6. Convergence Acceleration

The rate of convergence of a multistage scheme can be enhanced by residual averaging [3]. The general idea behind this technique is to replace the residual at one point in the flow field by a weighted average of the residuals at the neighboring points. The average is calculated implicitly.

In the one dimensional case it can be easily shown that a multistage scheme can be stabilized for an arbitrarily large value of the time step by choosing an appropriate value of the smoothing parameter ϵ . The analysis for the one dimensional non dissipative case [3] gives the following constraint:

$$\epsilon > \frac{1}{4} \left[\left[\frac{\Delta t}{\Delta t^*} \right]^2 - 1 \right] \quad (6.2)$$

where Δt^* is the maximum stable time step of the basic scheme and Δt is the actual time step.

The analysis in the 2-D case is more complicated. One simple way of extending the concept of residual averaging in 2-D is to consider the factorized form:

$$(1 - \epsilon_i \delta_{xx})(1 - \epsilon_j \delta_{yy}) \bar{R}_j = R_j \quad (6.3)$$

This form is particularly convenient since it only requires inversion of tridiagonal matrices. It has been proven to be effective for Euler computations, but generally less effective with the Navier Stokes equations. We will refer to this technique as residual averaging with constant coefficients, meaning that the smoothing parameters ϵ_i and ϵ_j are equal for every point in the flow field. The principal drawback is that the values for the smoothing parameters must be empirically determined and tuned.

To obviate this problem another strategy has been devised. This second technique will be referred to as residual averaging with locally varying coefficients, and it has been proved to be effective especially on highly stretched meshes. If we consider the model problem:

$$u_t + u_x + u_y = 0 \quad (6.4)$$

and we discretize the equation by central differencing, we have for a simple one stage scheme:

$$u^{n+1} = u^n - (\lambda_x \delta_{xx} u_i + \lambda_y \delta_{yy} u_j) \quad (6.5)$$

Taking the Fourier transform of eq(6.5) we get the following expression for the Fourier symbol:

$$f(\xi, \eta) = i(\lambda_x \sin \xi + \lambda_y \sin \eta) \quad (6.6)$$

where:

$$\xi = p \Delta x, \quad \eta = q \Delta y \quad (6.7)$$

$$\lambda_x = \frac{\Delta x}{\Delta t}, \quad \lambda_y = \frac{\Delta y}{\Delta t}$$

and the problem is reduced to

$$\frac{du}{dt} = f(\xi, \eta) u \quad (6.8)$$

in the transformed space. Consider now a factorized residual averaging of the form:

$$(1 - \epsilon_x \delta_{xx})(1 - \epsilon_y \delta_{yy}) \bar{R}_j = R_j \quad (6.9)$$

where δ_{xx} and δ_{yy} are central second difference operators in the two directions x and y , and ϵ_x and ϵ_y are locally varying smoothing parameters. Then the Fourier symbol will be replaced by:

$$f(\xi, \eta) = \frac{i(\lambda_x \sin \xi + \lambda_y \sin \eta)}{(1 + 2\epsilon_x(1 - \cos \xi))(1 + 2\epsilon_y(1 - \cos \eta))} \quad (6.10)$$

If $\xi=0$ or $\eta=0$ this reduces to the one dimensional case. The worst possible case is roughly when $\lambda_x = \lambda_y$ and $\xi = \eta$. Then the Fourier symbol (6.10) reduces to:

$$|f(\xi)| = \frac{2\lambda \sin \xi}{(1 + 2\epsilon(1 - \cos \xi))^2} \quad (6.11)$$

Now considering the points at which $d|f|/d\xi$ vanishes we are able to set an upper bound on the maximum growth factor in terms of the smoothing parameter ϵ as

$$|f|_{\max} < \left\{ \frac{(1 - \frac{4\epsilon}{1+4\epsilon})(1 + \frac{4\epsilon}{1+4\epsilon})}{(1 + \frac{4\epsilon}{1+8\epsilon})^2} \right\}^{1/2} \quad (6.12)$$

From this formula smoothing rules for the 2-D case can be established. If we define now the following modified wave speeds in the i and j directions of the computational plane:

$$\begin{aligned} \bar{\lambda}_i &= \phi(r) \lambda_i \\ \bar{\lambda}_j &= \phi\left(\frac{1}{r}\right) \lambda_j \end{aligned} \quad (6.13)$$

where $r = \lambda_i / \lambda_j$ and $\phi(r) = 1 + r^a$, then the choice of the smoothing parameters can be taken as:

$$\epsilon_i = \max \left\{ \frac{1}{4} \left[\left[\frac{\bar{\lambda}_i}{\lambda_i^*} \right]^2 - 1 \right], 0 \right\} \quad (6.14)$$

$$\epsilon_j = \max \left\{ \frac{1}{4} \left[\left(\frac{\lambda_j}{\lambda^*} \right)^2 - 1 \right], 0 \right\}$$

In practical computations it has been found that the coefficient $\alpha=2/3$ gives good results.

Convergence to a steady state is also enhanced by advancing in time each computational cell at its own maximum permissible time step as determined by a local stability analysis [5].

Radical further enhancement of the rate of convergence of the scheme is achieved by using the multigrid time stepping algorithm devised by Jameson [4]. Details of the method and its extension to the viscous form of the equations have been presented elsewhere [2,5]. It is worth mentioning, however, that a W-cycle has been employed in the multigrid scheme for all the calculations presented in this work.

7. Results with the Adaptive Dissipation Model

The ultimate goal of numerical computation is the prediction of the loads on aerodynamic bodies. The parameters of interest for the designer are the coefficients of lift, drag and moment. The computed aerodynamic characteristics of three airfoils (NACA 0012, RAE 2822, JONES - SUPERCRITICAL) are presented in this section. The five stage scheme with three evaluations of the dissipation is employed to drive the multigrid W-cycle [5]. Also implicit smoothing with locally varying coefficients is used. The CFL number is fixed at 7.5. For each of the cases presented the effect of mesh refinement is monitored by performing computations on a sequence of grids.

The free stream flow conditions, and angles of attack cover a wide range in the transonic regime. The results presented correspond to some of the mandatory and suggested cases of a recent Workshop [7] on the simulation of viscous flows, and comparisons are made with the results obtained by two other authors [11,12], and with experimental data, when available. These comparisons are summarized in Tables 1,2,3. Table 1 shows the comparison with experimental data, while Tables 2 and 3 show the comparisons with the results calculated by Coakley [11], and Maksymiuk and Pulliam [12]. In the tables, the computed values of the pressure drag coefficient C_{d_p} , friction drag coefficient C_{d_f} , and total drag coefficient C_{d_t} are reported separately. In the figures only the value of the pressure drag coefficient is reported.

A. NACA 0012

The typical mesh used for the computations on the NACA 0012 airfoil is shown in fig. (7.1). It consists of a total of 320x64 mesh cells. The number of points that are fitted on the airfoil is either 193 or 257. The minimum distance from the airfoil surface of the first coordinate line is 4×10^{-6} chords, and it corresponds to a value of $y^+ < 5$ for the assigned Re_∞ of 9×10^6 . Transition is fixed at .05 chords. Also the

outer boundary is placed at a distance of 20 chords.

The first set of computations is designed to recover the $C_l - \alpha$ curve, as well as the drag polar, corresponding to a free stream speed of $M_\infty = .7$. The computed $C_l - \alpha$ curve, and drag polar are shown, respectively, in fig. (7.2) and fig. (7.3), in which the experimental values obtained by Harris [13] are also marked for comparison. The computed data correlates extremely well with the experimental values corrected, using the criterion suggested by Harris, for wind tunnel interference. The linear region is recovered, and the computed results show a departure from linearity between $\alpha=4-5^\circ$. This behavior is caused by the growth of the shock induced separation region. The pressure plots corresponding to the four angles of attack are also shown in fig.(7.4). As the angle of attack is increased, the position of the shock wave is progressively shifted upstream while its strength

is increased considerably. At about 3° angle of attack, the shock is already strong enough to cause the formation of a separated region right at the wave foot. The results obtained in the present study compare quite well both with the experiments and with the results computed by other schemes, as summarized in Tables 1,2,3. The convergence histories measured by the decay of the RMS of the density residuals corresponding to these computations are also shown in fig.(7.5). Although it was found that the values of the aerodynamic coefficients are converged to the fourth decimal place in about 125 multigrid cycles, the computations were carried on further to 200 cycles to check the convergence properties of the scheme. A monotone reduction of the density residuals is observed in all the cases considered. This shows that the convergence of the scheme is fairly independent on the physical pattern of the flow field. For the case

corresponding to 5° angle of attack, convergence was found to be somewhat slower. When the stall conditions are approached, it is not certain that the flow will remain steady. However, in this case also, converged values (to the fourth decimal place) of the aerodynamic coefficients were obtained in about 120 multigrid cycles.

Qualitative and quantitative agreement with other computed results as well as with the experiment of Harris is also obtained for the next case presented, corresponding to a free stream speed of $M_\infty = .55$ and at 8.34° angle of attack. The presence of a large separation bubble is revealed by the computed pressure plot of fig.(7.6). Also for this case the convergence history is quite satisfactory (fig. 7.7), and convergence within engineering accuracy is achieved in about 120 multigrid cycles.

B. RAE 2822

Four cases were computed for the RAE 2822 airfoil. These cases correspond to the experimental conditions 1,6,9 and 10 of ref. [14]. Angle of attack corrections are extremely important for this airfoil. The most widely used

method of determining an appropriate correction is to tune the geometrical angle of attack [7,11,12] in such a way that the computed lift matches the experimental one. This criterion has been used for the computation of case 1. However, since the main purpose of this study is the validation of the numerical scheme, the remaining cases were computed with the angle of attack matching that which was used by other authors in the computations of the same test cases. The free stream conditions and the geometrical angles of attack that correspond to the four cases on this airfoil are again summarized in Tables 1,2,3. Also transition was fixed at the experimental locations. The calculations for cases 1 and 10 were performed on a 320x64 grid with 193 points fitted on the airfoil (fig. 7.8), while for cases 6 and 9 a finer 512x64 grid was employed (fig.7.9). The distance from the airfoil of the first grid line was chosen in such a way as to provide the necessary clustering of points in the boundary layer region. Again, the distance of the first mesh point was taken to satisfy the condition $y^+ < 5$.

Fig.(7.10) shows the computed pressure coefficient along the airfoil surface corresponding to case 1. The computed results are in fairly good agreement with the measurements. Note also that the computed aerodynamic coefficients are in excellent agreement with the experimental values (cfr. Tab 1). For this case the angle of attack correction that has been introduced is in close agreement with the correction computed using the criterion suggested by the experimental investigation. The flow remains fully attached, and the resolution provided by the 320x64 grid is sufficient for an adequate representation of the physical phenomena. The convergence history is shown in fig.(7.11). Again, the convergence rate is quite satisfactory, and a reduction of four orders of magnitude of the density residuals is achieved in 100 multigrid cycles. Also, a converged value of the lift coefficient is recovered in about 75 cycles.

The second computation corresponds to the experimental conditions of case 10. A 320x64 grid was again used. The geometrical angle of attack of the computation corresponds to the value used by Coakley [11]. The computed solution for this case is less satisfactory. The comparison of the surface pressure plot in fig.(7.12) with the experimental data reveals that the computed shock is too far downstream, and also that its strength is too great. A more detailed analysis of the computed flow field reveals that the flow is separated by the interaction of the shock and the boundary layer. Nevertheless, the solution computed with the present method compares favorably with other solutions computed with the same turbulence model [7]. The source of the disagreement must therefore be attributed to the poor reproduction of the shock boundary layer interaction with this turbulence model. Indeed, better agreement with the experiments has been obtained by Coakley using the Johnson and King model [11]. However, the performance of the multigrid scheme continues to be superior to other time stepping schemes even for this particular case. The convergence

history plot for the computation of this case (fig.7.13) confirms, once again, that the convergence properties of the scheme developed in this work are independent of the complexity of the flow pattern.

With the help of the first two cases presented, we have been able to show that while the Baldwin Lomax turbulence model gives a good reproduction of the flow field for attached flows (case 1), it fails to give an appropriate representation of a strong shock boundary layer interaction (case 10). Also we have proved that the numerical scheme developed in the present work is robust enough to handle complex flow fields. The next logical step is therefore to study the behavior of the numerical scheme for shocked flows where the turbulence model is able to give a reasonably good representation of the physics. The next two cases belong to this category. For these the finer 512x64 grid of fig.(7.9), with 385 points fitted on the airfoil has been used.

The surface pressure coefficient distribution for case 6 is shown in fig. (7.14). The agreement with the experiments is satisfactory.

At the geometrical angle of attack of 2.4° the shock position is found to be slightly upstream than the experimental one, but its strength compares favorably with the measurements. This suggests that the upstream location of the computed shock is attributable to the angle of attack correction used. For this case the convergence history is again quite satisfactory (fig. 7.15), and the computed results are also in agreement with other computations (Tables 2,3).

For the last case considered here (case 9), the location of the shock and the qualitative behavior of the surface pressure coefficient compares well with the experimental values (fig.7.16). The computed aerodynamic coefficients are in good agreement with other computations as summarized in the Tables, and the convergence history remains satisfactory fig.(7.17). A steady state solution, converged within engineering accuracy, is obtained in about 120 multigrid cycles.

In the course of this study we have been particularly concerned with the effect of the dissipation added in the scheme by second differencing. It turns out that the artificial dissipation does not interfere at all with the physical diffusion process. To prove this point case 9 was also run without any such dissipation. Fig.(7.18) shows that the pressure distribution computed for case 9 with the second differencing filter turned off is almost identical to the previous solution (fig.7.16). This seems to indicate that the distribution of the eddy viscosity predicted by the turbulence model is qualitatively accurate, and allows, by itself, the clean capture of the shock wave.

All the computations presented so far have been made using the theoretical coordinate definitions of the RAE 2822 airfoil. However, the wind tunnel experiments were performed with a physical model of the airfoil. As one would expect, therefore, the coordinates of the experimental section differ slightly from the

coordinates used in the computations. The next example will help to clarify the importance of the surface definition for comparisons between calculations and experimental data. Fig(7.19) shows the surface pressure plot obtained by using the physical coordinates of the wind tunnel model in the computation. Since in this case the surface definition is no longer smooth, several bumps in the computed solution are noticeable. The most interesting feature of these results, however, is that the leading edge suction is noticeably increased. This suggests that part of the disagreement between computed solutions and experimental values, in the leading edge region, may be attributable to the coordinate definition of the airfoil.

C. JONES SUPERCRITICAL AIRFOIL

This airfoil is a supercritical wing section designed by R.T. Jones. No experimental data for this section is available for comparison. However, since other computed solutions are available, it was decided to test the performance of our numerical method for this airfoil also. The free stream conditions and the values of the computed aerodynamic coefficients are summarized in Tables 1,2,3. The mesh is made up by 512x64 cells with 385 points fitted on the airfoil (fig.7.20). The computed pressure coefficient along the surface is plotted in fig.(7.21). The results obtained are in good agreement with other computations [7]. The convergence for this case is, once again, satisfactory (fig.7.22), and a steady state solution is obtained in about 120 multigrid cycles.

These results for three different wing sections validate the numerical scheme developed in the present work in comparison with other computed results and experimental measurements. Throughout the study the method has been proven robust, and to be capable of handling different flow patterns corresponding to a wide range of free stream conditions. The rate of convergence has also been shown to be fairly independent from the complexity of the flow. It has been shown that predictions using the Baldwin and Lomax model agree fairly well with experimental data when the flow is attached or only slightly separated. When the shock wave is strong enough to separate the flow, the model tends to overpredict the extent of the separated region. This results in the prediction of a stronger shock located too far downstream. Not only is the reproduction of the physics inadequate there, but also there is an increased possibility of failure of the numerical scheme through a discontinuous prediction of the eddy diffusivity. It seems that a differential model would be desirable for both physical and numerical purposes. Since the numerical algorithm is fully vectorizable, the increase in the computational effort incurred by the introduction of a two-equation model should not exceed 30%.

B. Validation of the Basic Scheme with the Flux Limited Dissipation

Solutions of three test cases for the RAE 2822 airfoil obtained by making use of the flux limited dissipation model are presented next. The free stream conditions and angles of attack

corresponds to those of cases 6, 9 and 10 of Ref [14] and have been already described in the previous section. The calculations have been performed both on the 512x64 grid shown in fig (8.1) and on a coarser 256x32 grid obtained by eliminating alternate points in the radial and wrap around direction. The normal to the wall distance of the first point in the outward direction is again taken as 2×10^{-5} chords.

The comparison between the pressure distribution computed on the finest grid and the experimental data is again favorable, as it is shown in figs (8.2a, 8.2b) for the attached and mildly separated transonic flows [case 6,9]. Also, for these cases, the solution computed by making use of the flux limited dissipation model agrees quite well with the results obtained with the adaptive dissipation (fig 7.14, 7.16).

On the other hand, when the flow is separated by the strong interaction of the shock with the boundary layer [case 10], the solution computed by making use of the flux limited dissipation deviates from the experiments (fig 8.2c) to the same extent as the solution computed with the adaptive dissipation model (fig 7.12). This again confirms, that for the particular flow conditions of case 10, the reason for the disagreement between computations and experiments must be sought in the definition of the turbulence model rather than in the accuracy of the numerical scheme.

The computed results for the coarser 256x32 grid shown in figs (8.3) are also in good agreement with the experiments and with the solutions obtained on the finest grid for all the three cases. This might be of importance for three dimensional applications where currently available computer do not allow the use of superfine grids. Also, since the computational cost of the flux limited dissipation model exceed the cost of the adaptive dissipation model by approximately 60%, only a better accuracy on coarser grids could make the flux limited model competitive for steady state calculations.

Finally, it should be noted that the multigrid algorithm maintains its excellent convergence properties in conjunction with the flux limited dissipation model. For all the calculations of this section a solution within engineering accuracy (aerodynamic coefficients converged to the third significant figure) is obtained in no more than 100 multigrid cycles independently of the dissipative model employed and the characteristics of the flow field.

Conclusion

Applications of a multigrid method to the Reynolds averaged equations have been presented for a variety of 2-D transonic flows. Two alternative formulations of the upwind biasing terms have been implemented. The results of these computations exhibit excellent agreement with the results of calculations by other numerical schemes using the same turbulence model. For attached flows good agreement with experiment data is also obtained. When the shock boundary layer interaction becomes strong enough to cause significant separation, the error

associated with the modeling of the turbulence exceeded by far the error associated with the numerical discretization scheme. The efficiency of the multigrid algorithm has been demonstrated, and results within engineering accuracy can be obtained in a small number of cycles. The combination of accuracy and speed of the multigrid time stepping scheme provides an essential tool for the study of turbulence modeling for aerodynamic flow, by making it possible to investigate alternative models and obtain a rapid and reliable assessment of their effects.

References

1. Jameson, A., "Successes and Challenges in Computational Aerodynamics", AIAA 87-1184-CP, June 1987.
2. Martinelli, L., Jameson, A. and Grasso, F., "A Multigrid Method for the Navier-Stokes Equations", AIAA Paper 86-0208, January 1986.
3. Jameson, A., "Transonic Flow Calculations", Princeton University Report, MAE 1651, 1984, included in Lecture Notes in Mathematics, 1127, edited by F. Brezzi, Springer Verlag, 1985, pp. 156-242.
4. Jameson, A., "Multigrid Algorithms for Compressible Flow Calculations", MAE Report 1743, Text of Lecture given at 2nd European Conference on Multigrid Methods, Cologne, October 4, 1985.
5. Martinelli, L., "Calculations of Viscous Flows with a Multigrid Method", Princeton University, MAE Dept., Ph.D Thesis 1754T, June 1987.
6. Jameson, A., "A Non-Oscillatory Shock Capturing Scheme Using Flux Limited Dissipation", MAE Report 1653.
7. Holst, T.L., "Viscous Transonic Airfoil Workshop Compendium of Results", AIAA Paper 87-1460, 1987.
8. Rubesin, M.W. and Rose, W.C., "The Turbulent Mean-Flow, Reynolds-Stress, and Heat-Flux Equations in Mass-Averaged Dependent Variables", NASA-TM-X-62248, March 1973.
9. Baldwin, B.S. and Lomax, H., "Thin Layer Approximation and Algebraic Model for Separated Turbulent Flows", AIAA Paper 78-275, 1978.
10. Roe, P.L., "Approximate Riemann Solvers, Parameter Vectors, and Difference Schemes", Journal of Comp. Physics, 43, pp. 357-372, 1981.
11. Coakley, T.J., "Numerical Simulation of Viscous Transonic Airfoil Flows", AIAA Paper 87-0416, 1987.
12. Maksymiuk, C.M. and Pulliam, T.H., "Viscous Transonic Workshop Results Using Arc2d", AIAA Paper 87-0415, 1987.
13. Harris, D.H., "Two Dimensional Aerodynamic Characteristics of the NACA 0012 Airfoil in the Langley 8-foot Transonic Pressure Tunnel", NASA-TM-81927, April 1981.
14. Cook, P.H., Mc Donald, M.A. and Firmin, M.C.P., "AEROFOIL RAE 2822 Pressure Distributions, Boundary Layer and Wake Measurements", AGARD Advisory Report No. 138, 1979.

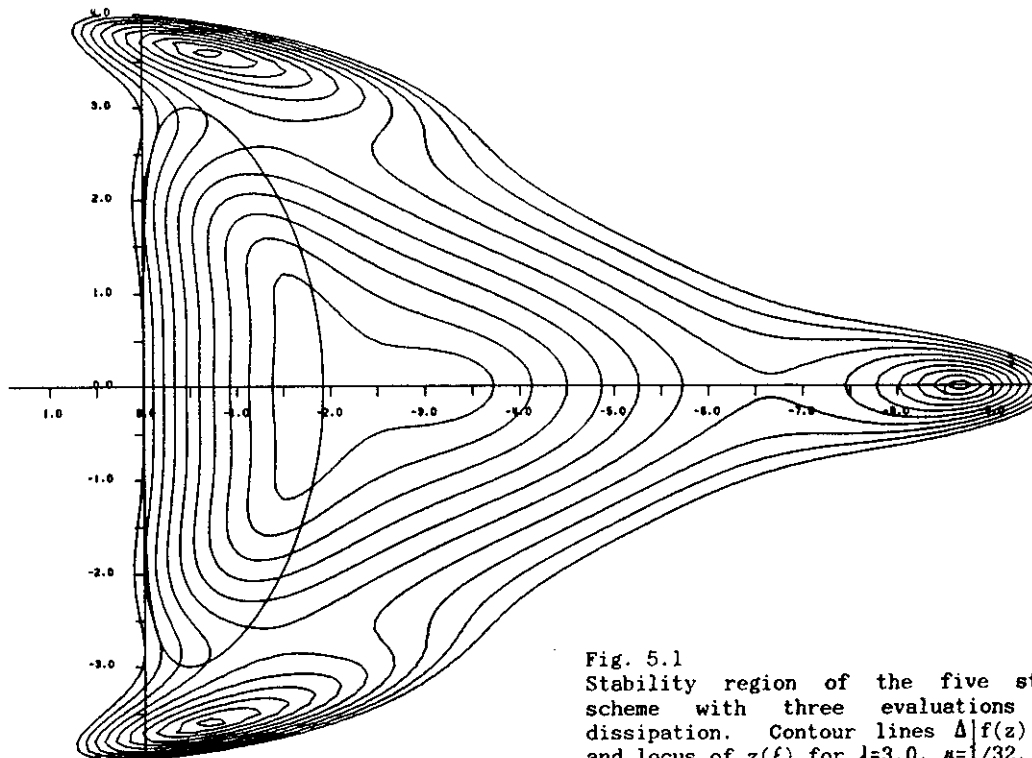


Fig. 5.1
Stability region of the five stage scheme with three evaluations of dissipation. Contour lines $\Delta|f(z)|=1$ and locus of $z(\xi)$ for $\lambda=3.0$, $\mu=1/32$.

TABLE 1

NACA 0012		Transition fixed at .05 chords						Experiments (Ref. 13)		
CASE	M_∞	θ_c	Re_∞	C_l	C_{d_p}	C_{d_f}	C_{d_t}	σ	C_l	C_d
1	.7	1.49	9×10^6	.2517	.0022	.0059	.0081	1.86	.241	.0079
2	.7	3.00	9×10^6	.4836	.0090	.0059	.0150			
3	.7	4.00	9×10^6	.6445	.0207	.0043	.0256			
4	.7	5.00	9×10^6	.7577	.0378	.0045	.0423			
5	.55	8.34	9×10^6	.9907	.0323	.00389	.0367	9.86	.983	.0253
RAE 2822		Transition fixed at .03 chords (.11 for case 1)						Experiments (Ref. 14)		
1	.676	1.83	5.7×10^6	.5677	.0031	.0073	.0104	2.40	.566	.0085
6	.725	2.4	6.5×10^6	.7601	.0062	.0062	.0124	2.92	.743	.0127
9	.730	2.79	6.5×10^6	.8415	.0121	.0059	.0181	3.19	.803	.0168
10	.750	2.81	6.2×10^6	.8650	.0247	.0073	.0320	3.19	.743	.0242
JONES										
1	.75	2.0	9×10^6	.5623	.0120	.0054	.0174			

TABLE 2

NACA 0012		Transition fixed at .05 chords						Computations (Ref 11)		
CASE	M_∞	θ_c	Re_∞	C_l	C_{d_p}	C_{d_f}	C_{d_t}	σ	C_l	C_d
1	.7	1.49	9×10^6	.2517	.0022	.0059	.0081	1.49	.255	.0083
2	.7	3.00	9×10^6	.4836	.0090	.0059	.0150	3.00	.504	.0142
3	.7	4.00	9×10^6	.6445	.0207	.0043	.0256			
4	.7	5.00	9×10^6	.7577	.0378	.0045	.0423	5.00	.766	.0428
5	.55	8.34	9×10^6	.9907	.0323	.00389	.0367	8.34	.994	.0358
RAE 2822		Transition fixed at .03 chords (.11 for case 1)								
1	.676	1.83	5.7×10^6	.5677	.0031	.0073	.0104	1.93	.620	.0087
6	.725	2.4	6.5×10^6	.7601	.0062	.0062	.0124	2.40	.788	.0124
9	.730	2.79	6.5×10^6	.8415	.0121	.0059	.0181	2.80	.861	.0185
10	.750	2.81	6.2×10^6	.8650	.0247	.0073	.0320	2.80	.859	.0298
JONES										
1	.75	2.0	9×10^6	.5623	.0120	.0054	.0174	2.00	.576	.0178

TABLE 3

NACA 0012	Transition fixed at .05 chords							Computations (Ref 12)		
CASE	M_∞	α_c	Re_∞	C_l	C_{d_p}	C_{d_f}	C_{d_t}	σ	C_l	C_d
1	.7	1.49	9×10^6	.2517	.0022	.0059	.0081			
2	.7	3.00	9×10^6	.4836	.0090	.0059	.0150	3.00	.503	.0144
3	.7	4.00	9×10^6	.6445	.0207	.0043	.0256			
4	.7	5.00	9×10^6	.7577	.0378	.0045	.0423	5.00	.763	.0431
5	.55	8.34	9×10^6	.9907	.0323	.00389	.0367	8.34	.988	.0362
RAE 2822	Transition fixed at .03 chords (.11 for case 1)									
1	.676	1.83	5.7×10^6	.5677	.0031	.0073	.0104			
6	.725	2.4	6.5×10^6	.7601	.0062	.0062	.0124			
9	.730	2.79	6.5×10^6	.8415	.0121	.0059	.0181			
10	.750	2.81	6.2×10^6	.8650	.0247	.0073	.0320	2.72	.838	.0289
JONES										
1	.75	2.0	9×10^6	.5623	.0120	.0054	.0174	2.00	.558	.0178

Tables 1, 2 and 3 - *legenda*

M_∞ = Free stream Mach number

α_c = Angle of attack (degrees) used in the computation

Re_∞ = Reynolds number based on chord and free stream conditions

C_l = Lift coefficient

C_{d_p} = Pressure drag coefficient

C_{d_f} = Friction drag coefficient

C_{d_t} = Total drag coefficient

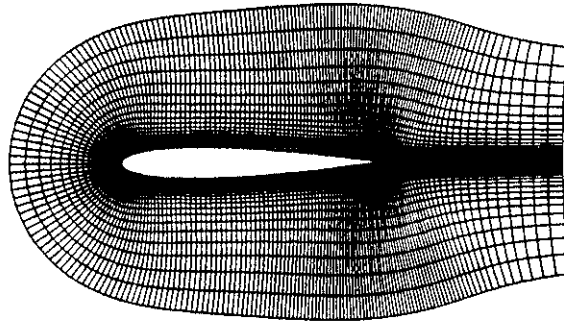


Fig. 7.1
 NACA 0012 airfoil -
 320x64 C-mesh for turbulent
 computations.

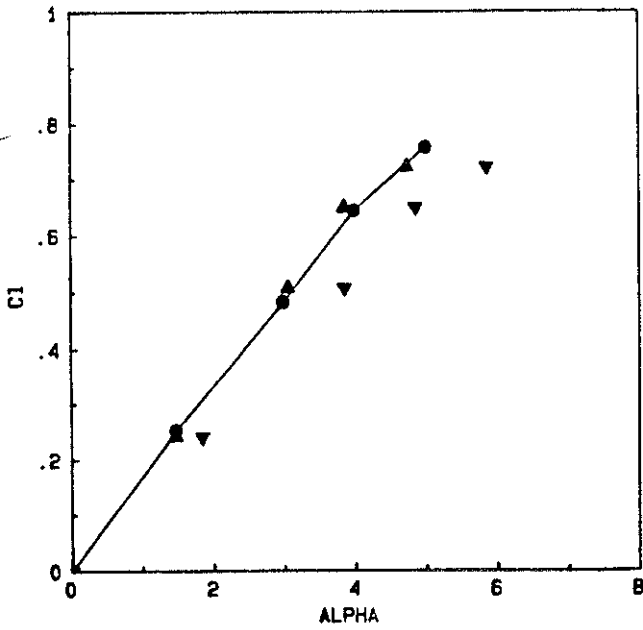


Fig. 7.2
 NACA 0012 airfoil - C_l - α plot
 $M_\infty = .7$
 $Re_\infty = 9 \times 10^6$
 Transition fixed at .05 chords
 ● COMPUTED
 ▼ UNCORRECTED EXPERIMENTS (Ref. 13)
 ▲ CORRECTED EXPERIMENTS (Ref. 13)

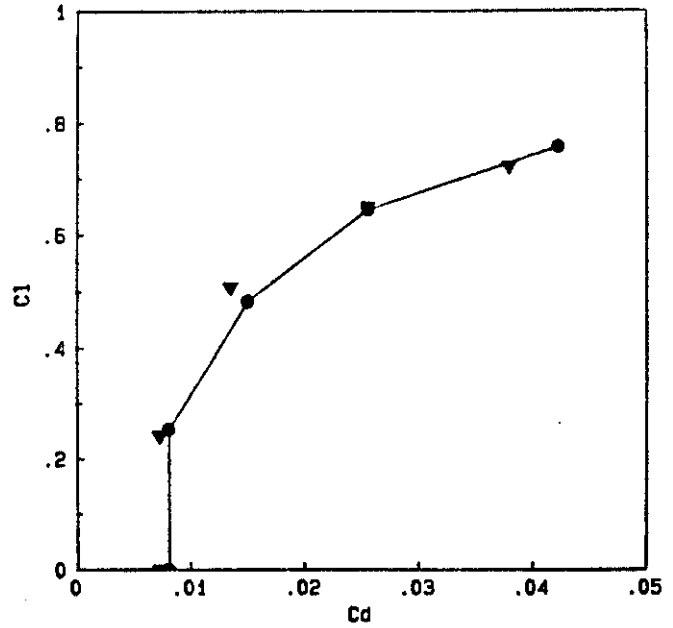
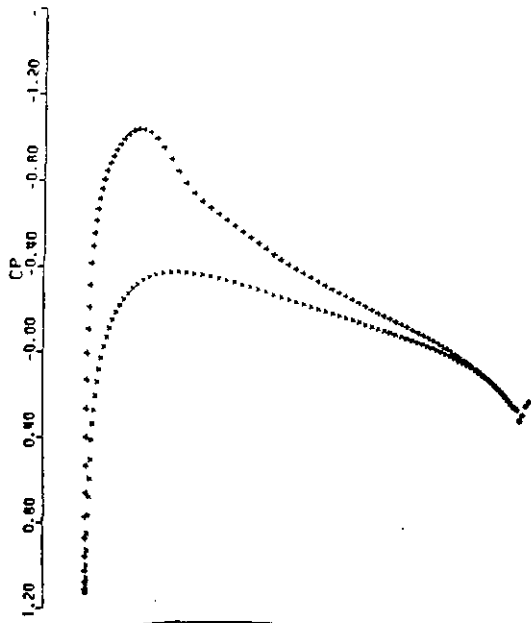
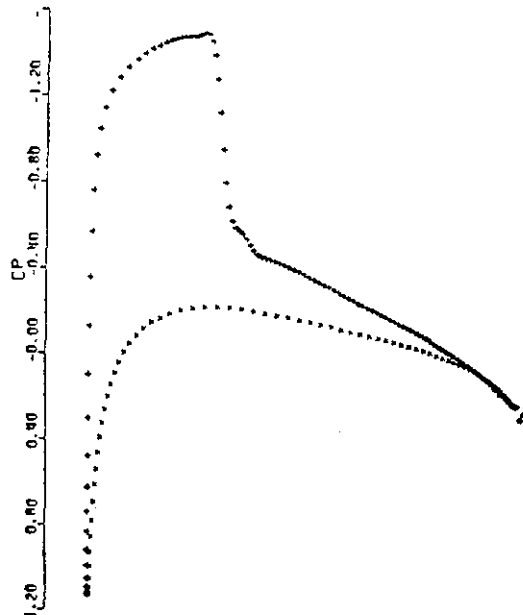


Fig. 7.3
 NACA 0012 airfoil - C_l - C_d plot
 $M_\infty = .7$
 $Re_\infty = 9 \times 10^6$
 Transition fixed at .05 chords
 ● COMPUTED
 ▼ EXPERIMENTS (Ref. 13)



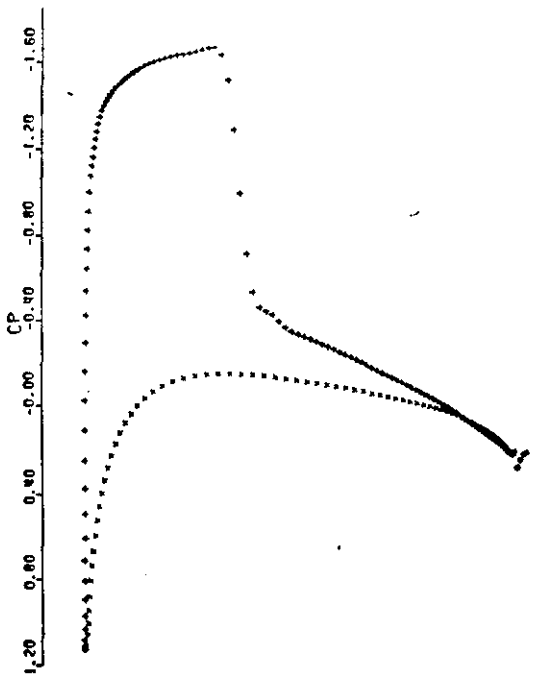
NACA0012 W-CYCLE TURBULENT CCS-A
 MACH 0.700 ALPHA 1.490
 CL 0.2517 CD 0.0022 CM 0.0043
 GRID 320X64 NCTC 200 RESO.400E-03

Fig. 7.4a
 NACA 0012 case (1)
 Computed Pressure coefficient along the surface.



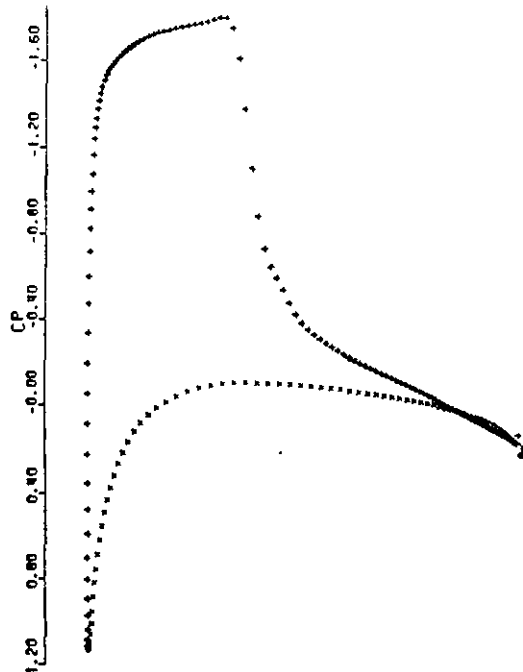
NACA0012 W-CYCLE TURBULENT CCS-A
 MACH 0.700 ALPHA 3.000
 CL 0.5006 CD 0.0088 CM 0.0135
 GRID 320X64 NCTC 200 RESO.100E-03

Fig. 7.4b
 NACA 0012 case (2) - CCS - A
 Computed Pressure coefficient along the surface.



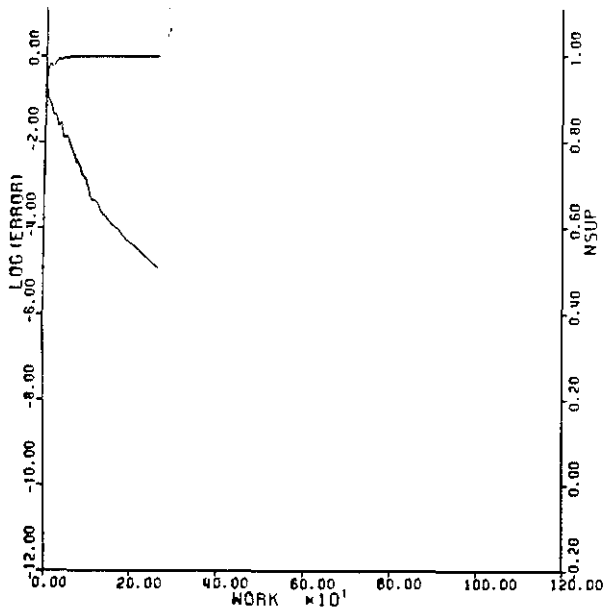
NACA0012 W-CYCLE TURBULENT CCS-A
 MACH 0.700 ALPHA 4.000
 CL 0.6445 CD 0.0207 CM 0.0176
 GRID 320X64 NCTC 125 RESO.660E-02

Fig. 7.4c
 NACA 0012 case (3)
 Computed Pressure coefficient along the surface.



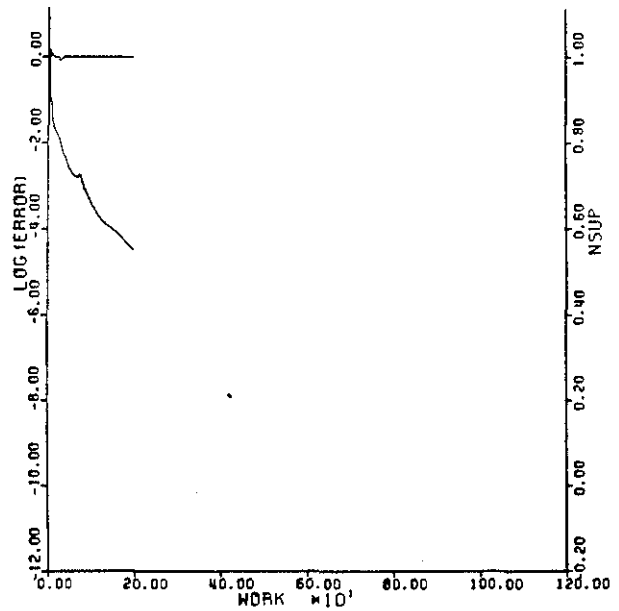
NACA0012 W-CYCLE TURBULENT CCS-A
 MACH 0.700 ALPHA 5.000
 CL 0.7581 CD 0.0378 CM 0.0189
 GRID 320X64 NCTC 300 RESO.215E-01

Fig. 7.4d
 NACA 0012 case (4)
 Computed Pressure coefficient along the surface.



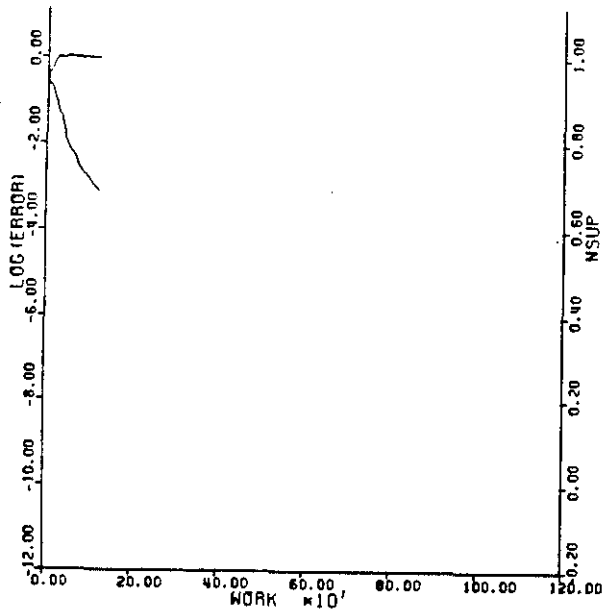
NACA0012 W-CYCLE TURBULENT CCS-A
MACH 0.700 ALPHA 3.000
RESID1 0.659E+01 RESID2 0.783E-04
WORK 265.58 RATE 0.9582
GRID 320X64

Fig. 7.5a
NACA 0012 case (1)
Convergence History.



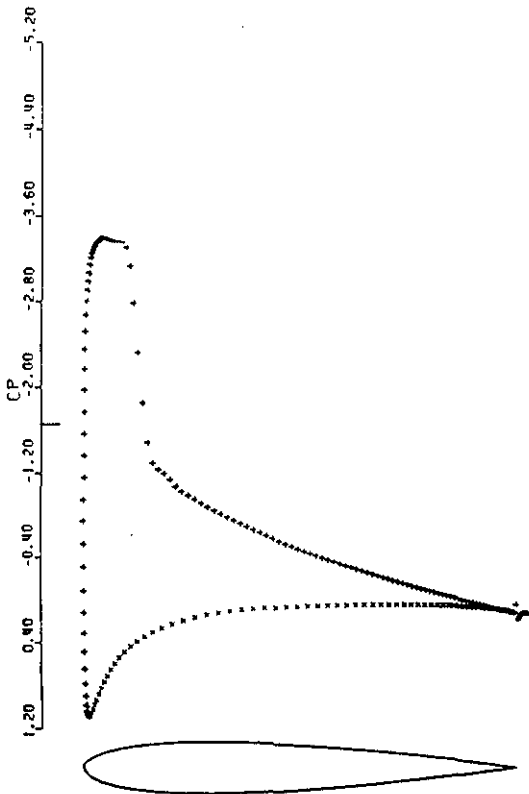
NACA0012 W-CYCLE TURBULENT CCS-A
MACH 0.700 ALPHA 1.490
RESID1 0.116E+02 RESID2 0.375E-03
WORK 199.00 RATE 0.9494
GRID 320X64

Fig. 7.5b
NACA 0012 case (2)
Convergence History.



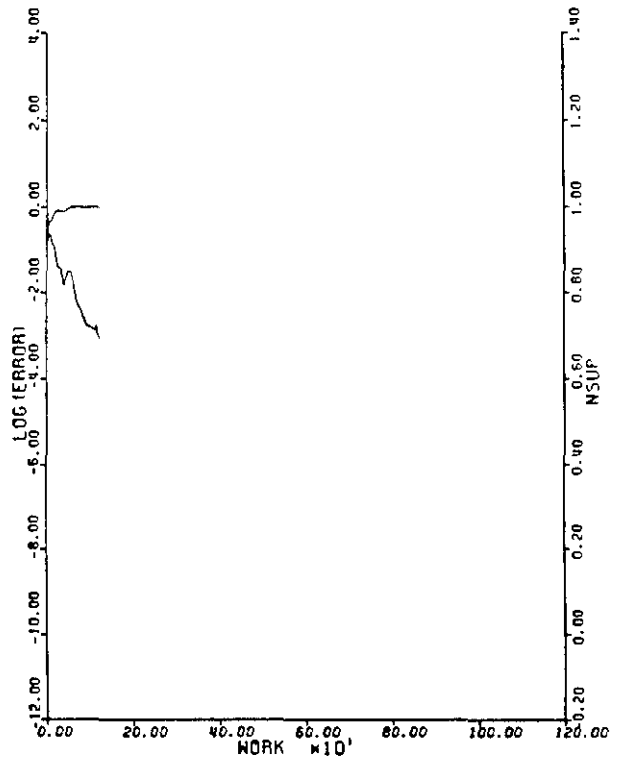
NACA0012 W-CYCLE TURBULENT CCS-A
MACH 0.700 ALPHA 4.000
RESID1 0.850E+01 RESID2 0.660E-02
WORK 124.00 RATE 0.9439
GRID 320X64

Fig. 7.5c
NACA 0012 case (3)
Convergence History.



NACA0012 W-CYCLE TURBULENT CCS-A
 MACH 0.550 ALPHA 8.340
 CL 0.9907 CD 0.0323 CM 0.0364
 GRID 320X64 NCTC 125 RESD.840E-02

Fig. 7.6
 NACA 0012 case (5)
 Computed Pressure coefficient along the surface.



NACA0012 W-CYCLE TURBULENT CCS-A
 MACH 0.550 ALPHA 8.340
 RESID1 0.957E+01 RESID2 0.839E-02
 WORK 124.00 RATE 0.9448
 GRID 320X64

Fig. 7.7
 NACA 0012 case (5)
 Convergence History.

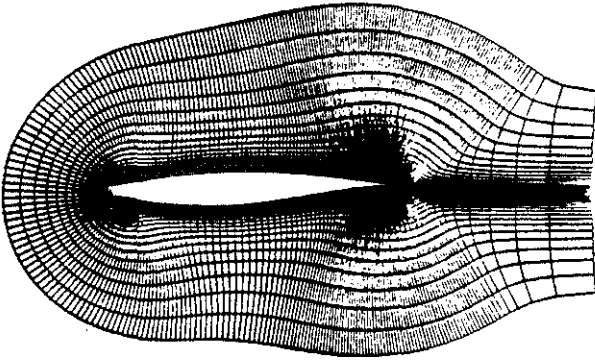


Fig. 7.8
RAE 2822 airfoil
320x64 grid for turbulent calculations.

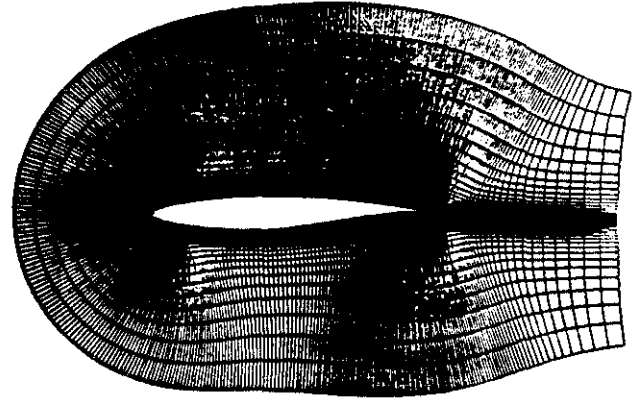
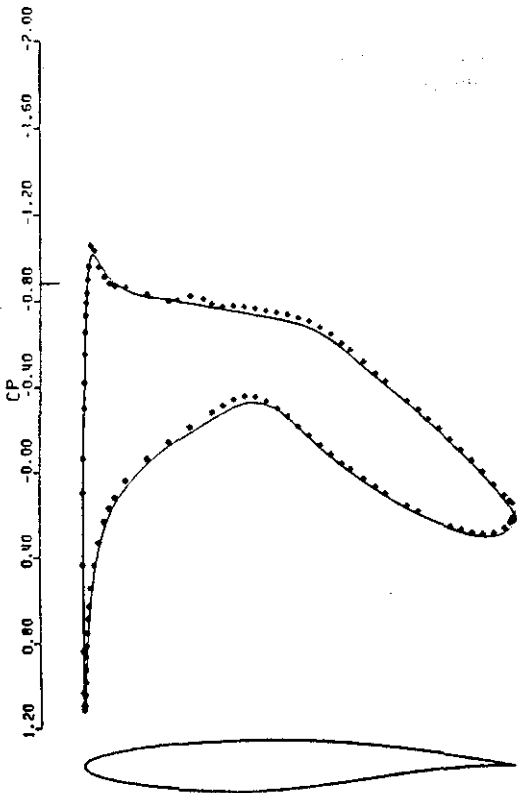
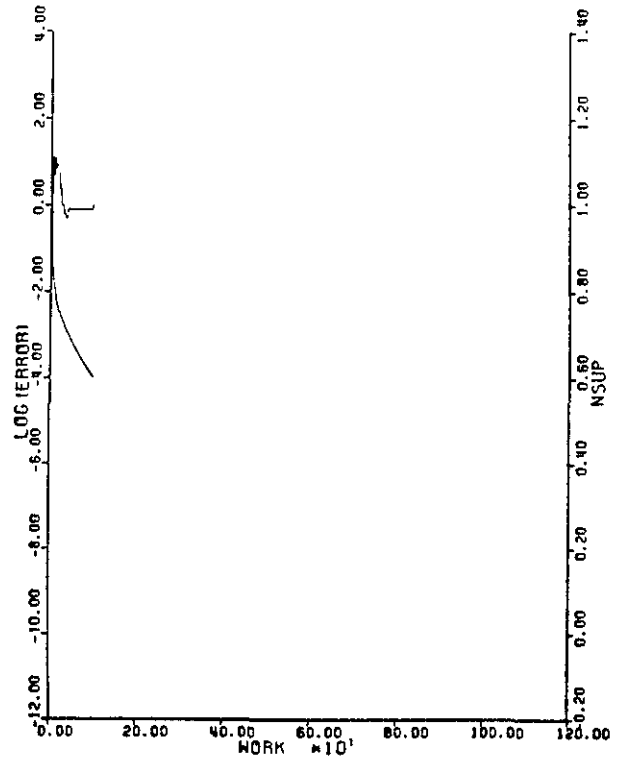


Fig. 7.9
RAE 2822 airfoil
512x64 grid for turbulent calculations.



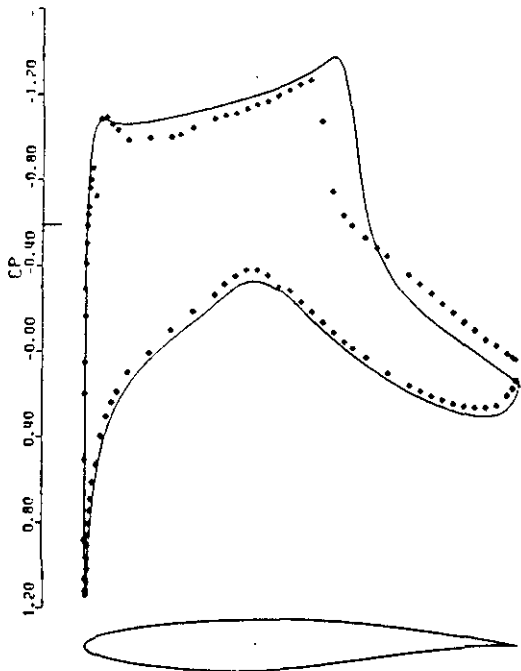
RAE2822 W-CYCLE TURBULENT # 1
MACH 0.676 ALPHA 1.890
CL 0.5677 CD 0.0031 CM -0.0807
GRID 320X64 NCYC 100 RESO.700F-03

Fig. 7.10
RAE 2822 airfoil case (1)
Pressure coefficient along the surface.
Solid line - Computed solution
* - Experiments (Ref. 14)



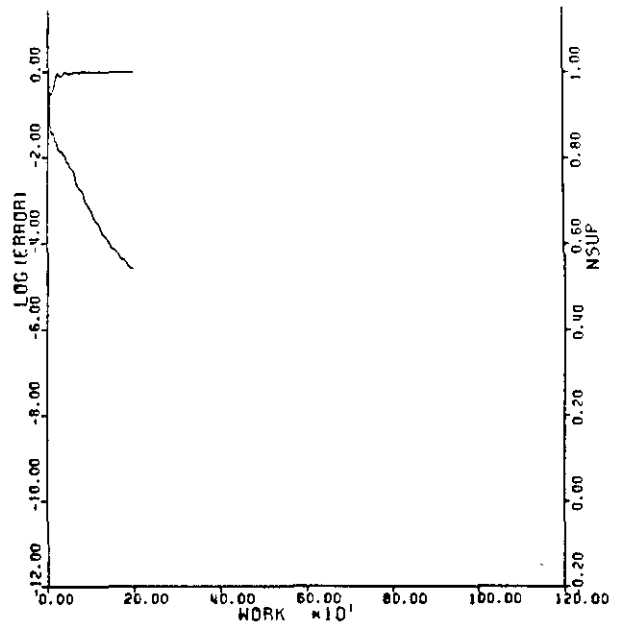
RAE2822 W-CYCLE TURBULENT # 1
MACH 0.676 ALPHA 1.890
RESID1 0.692E+01 RESID2 0.714E-03
WDK 99.00 RATE 0.9114
GRID 320X64

Fig. 7.11
RAE 2822 airfoil case (1)
Convergence History.



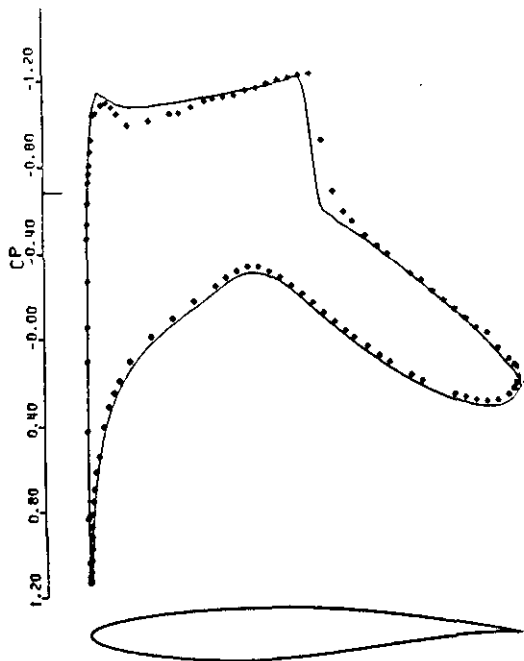
RAE2822 W-CYCLE TURBULENT = 10
 MACH 0.750 ALPHA 2.800
 CL 0.8404 CD 0.0231 CM -0.1139
 GRID 320X64 NCYC 200 RESO.200E-03

Fig. 7.12
 RAE 2822 airfoil case (10)
 Pressure coefficient along the surface.
 Solid line - Computed solution
 * - Experiments (Ref. 14)



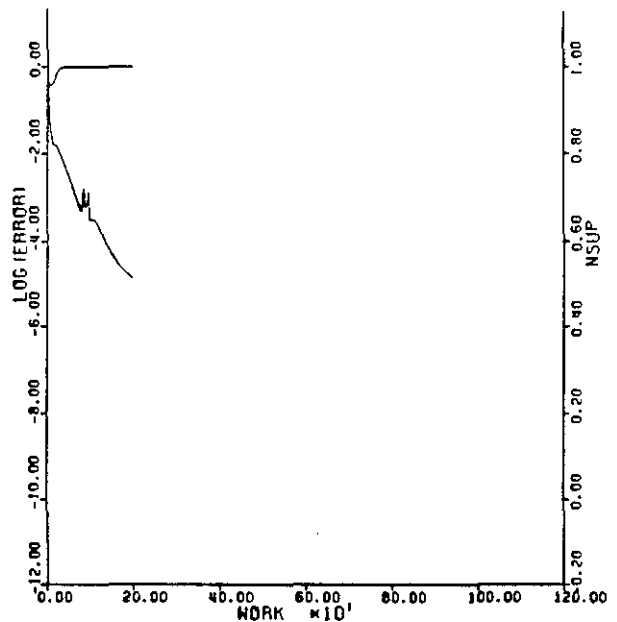
RAE2822 W-CYCLE TURBULENT = 10
 MACH 0.750 ALPHA 2.800
 RESID1 0.875E+01 RESID2 0.231E-03
 WORK 199.00 RATE 0.9484
 GRID 320X64

Fig. 7.13
 RAE 2822 airfoil case (10)
 Convergence History.



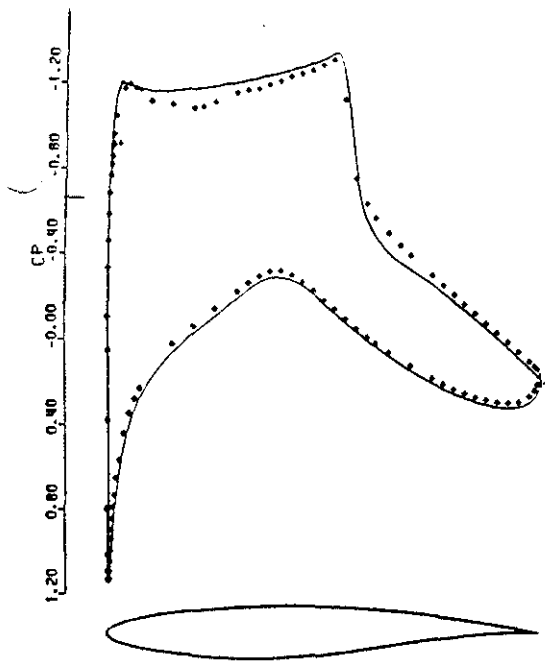
RAE2822 W-CYCLE TURBULENT = 6 BL
 MACH 0.725 ALPHA 2.400
 CL 0.7601 CD 0.0062 CM -0.0906
 GRID 512X64 NCYC 200 RESO.100E-03

Fig. 7.14
 RAE 2822 airfoil case (6)
 Pressure coefficient along the surface.
 Solid line - Computed solution
 * - Experiments (Ref. 14)



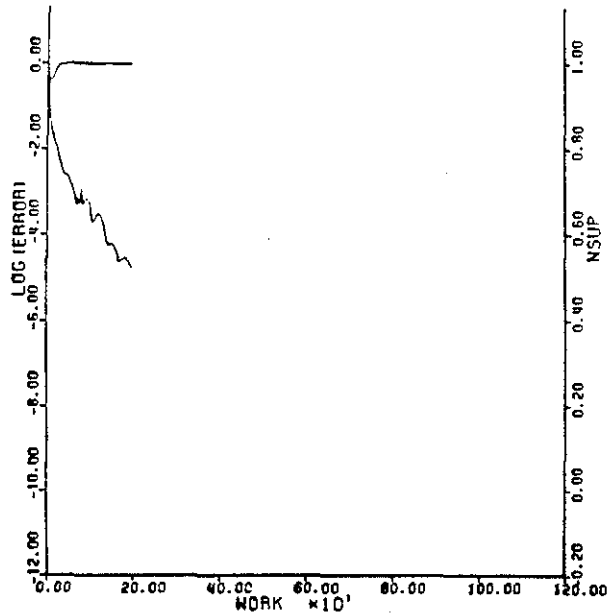
RAE2822 W-CYCLE TURBULENT = 6 BL
 MACH 0.725 ALPHA 2.400
 RESID1 0.113E+02 RESID2 0.149E-03
 WORK 199.00 RATE 0.9451
 GRID 512X64

Fig. 7.15
 RAE 2822 airfoil case (6)
 Convergence History.



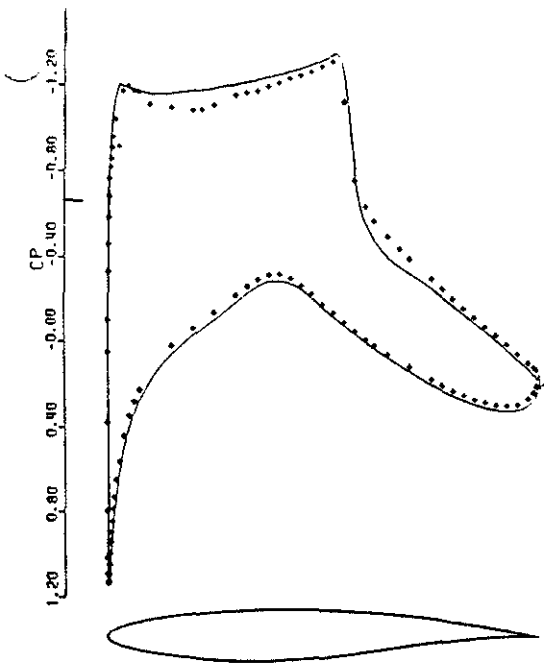
RAE2822 W-CYCLE TURBULENT * 8 BL
 MACH 0.730 ALPHA 2.790
 CL 0.8415 CD 0.0121 CM -0.0960
 GRID 512X64 NCYC 200 RESO.200E-03

Fig. 7.16
 RAE 2822 airfoil case (9)
 Pressure coefficient along the surface.
 Solid line - Computed solution
 * - Experiments (Ref. 14)



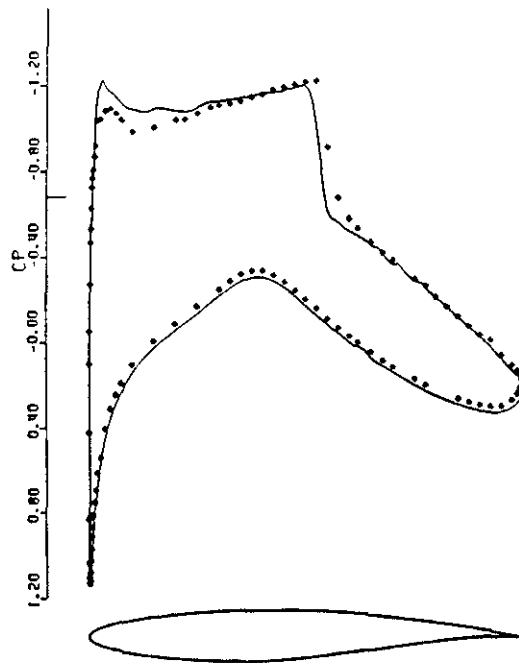
RAE2822 W-CYCLE TURBULENT * 9 BL
 MACH 0.730 ALPHA 2.790
 RESID1 0.117E+02 RESID2 0.195E-03
 WORK 199.00 RATE 0.9462
 GRID 512X64

Fig. 7.17
 RAE 2822 airfoil case (9)
 Convergence History.



RAE2822 W-CYCLE TURBULENT * 9 BL VIS2 = 0.
 MACH 0.730 ALPHA 2.790
 CL 0.8424 CD 0.0122 CM -0.0962
 GRID 512X64 NCYC 200 RESO.400E-03

Fig. 7.18
 RAE 2822 airfoil case (9)
 Pressure coefficient along the surface.
 Solid line - Computed solution
 * - Experiments (Ref. 14)



RAE2822-EX W-CYCLE TURBULENT * 6 BL
 MACH 0.725 ALPHA 2.400
 CL 0.7707 CD 0.0063 CM -0.0923
 GRID 512X64 NCYC 200 RESO.340E-02

Fig. 7.19
 RAE 2822 airfoil case (6)
 Pressure coefficient along the surface.
 Solid line - Computed solution
 * - Experiments (Ref. 14)

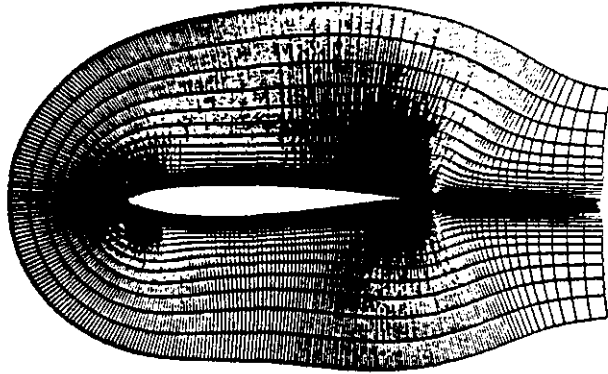
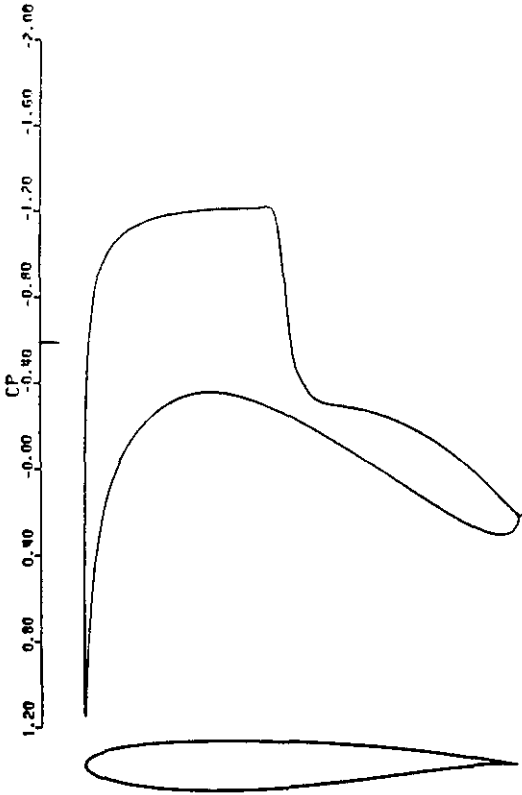
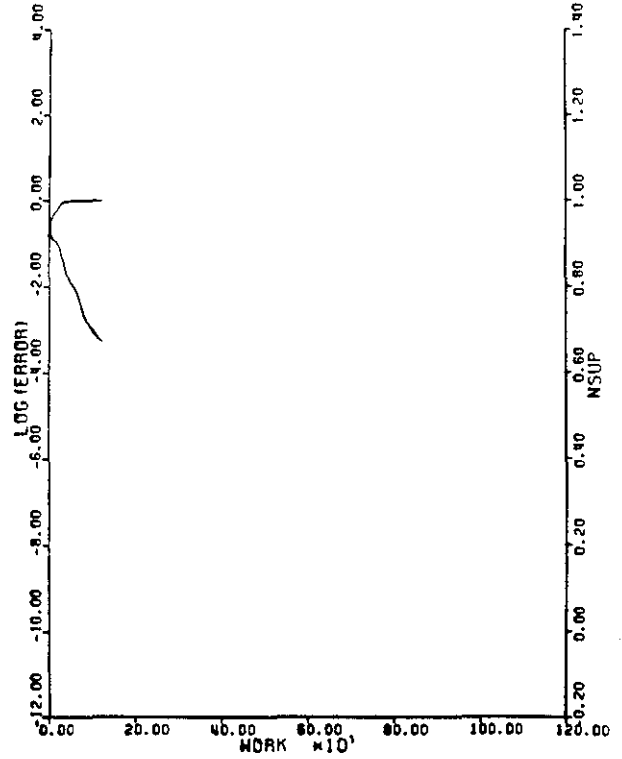


Fig. 7.20
 JONES airfoil
 512x64 grid for turbulent calculations.



JONES W-CYCLE TURBULENT * 1 CCS -A
 MACH 0.750 ALPHA 2.000
 CL 0.5623 CD 0.0120 CM -0.0492
 GRID 512X64 NCYC 125 RESO.230E-02

Fig. 7.21
 JONES airfoil
 Pressure coefficient along the surface.
 Solid line - Computed solution



JONES W-CYCLE TURBULENT * 1 CCS -A
 MACH 0.750 ALPHA 2.000
 RESID1 0.490E+01 RESID2 0.231E-02
 WORK 124.00 RATE 0.9411
 GRID 512X64

Fig. 7.22
 JONES airfoil
 Convergence History.

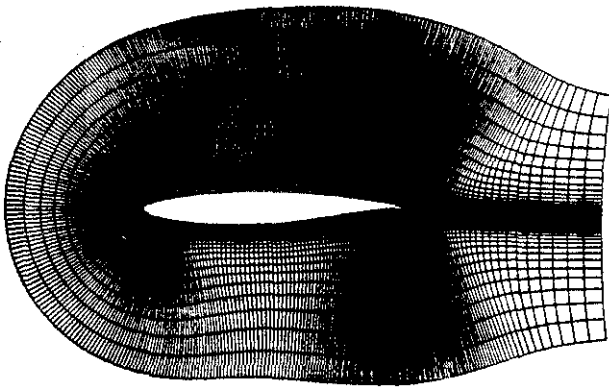
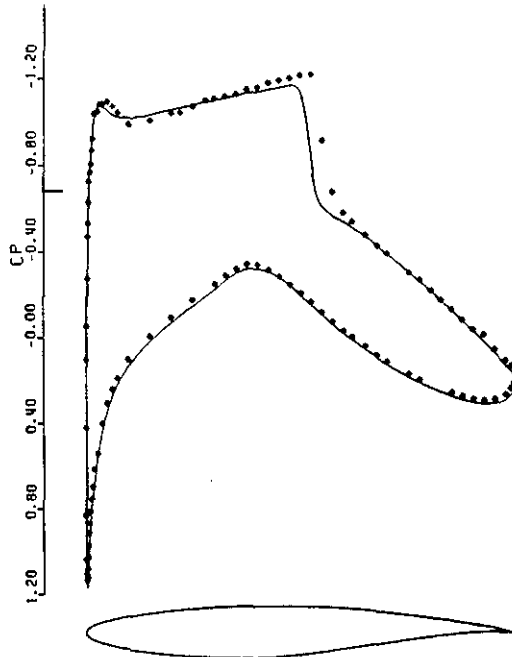
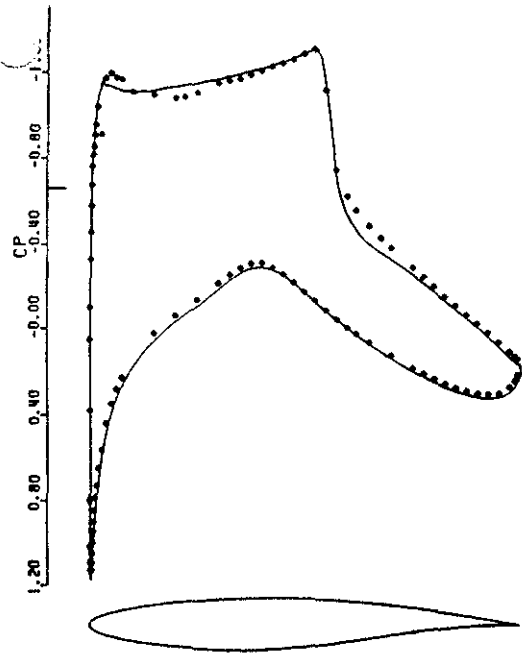


Fig. 8.1
RAE 2822 airfoil
512x64 grid for turbulent calculations.



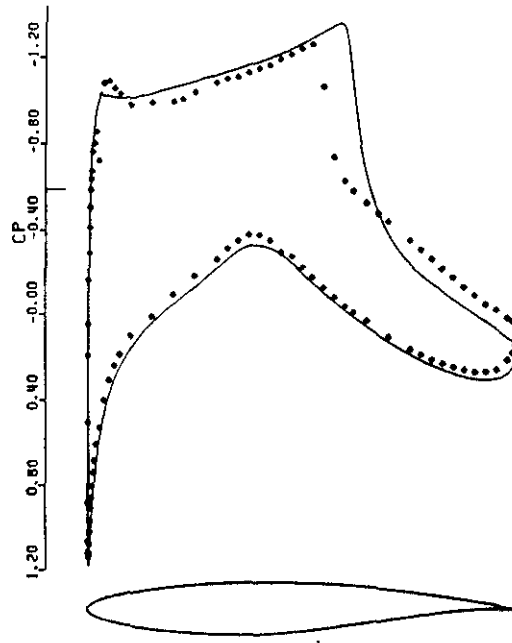
RAE2822 W-CYCLE TVD = 6
MACH 0.725 ALPHA 2.400
CL 0.7341 CD 0.0104 CM -0.0903
GRID 512X64 NCTC 75 RES0.490E-02

Fig. 8.2a
RAE 2822 airfoil case (6)
Pressure coefficient along the surface.
(Flux Limited dissipation model)
Solid line - Computed solution
* - Experiments (Ref. 14)



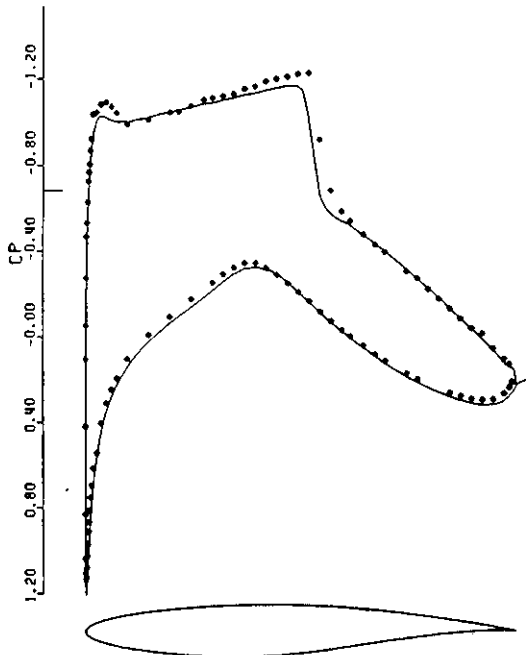
RAE2822 W-CYCLE TVD = 9
MACH 0.730 ALPHA 2.790
CL 0.8151 CD 0.0159 CM -0.0953
GRID 512X64 NCTC 75 RES0.460E-02

Fig. 8.2b
RAE 2822 airfoil case (9)
Pressure coefficient along the surface.
(Flux Limited dissipation model)
Solid line - Computed solution
* - Experiments (Ref. 14)



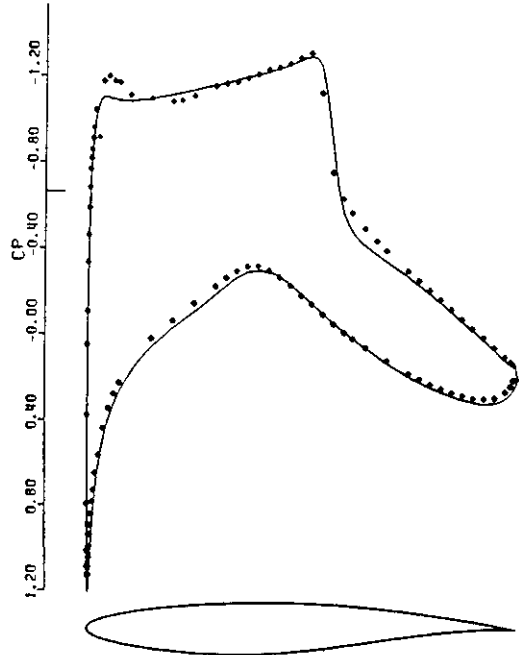
RAE2822 W-CYCLE TVD = 10
MACH 0.750 ALPHA 2.810
CL 0.8244 CD 0.0272 CM -0.1147
GRID 512X64 NCTC 75 RES0.830E-02

Fig. 8.2c
RAE 2822 airfoil case (10)
Pressure coefficient along the surface.
(Flux Limited dissipation model)
Solid line - Computed solution
* - Experiments (Ref. 14)



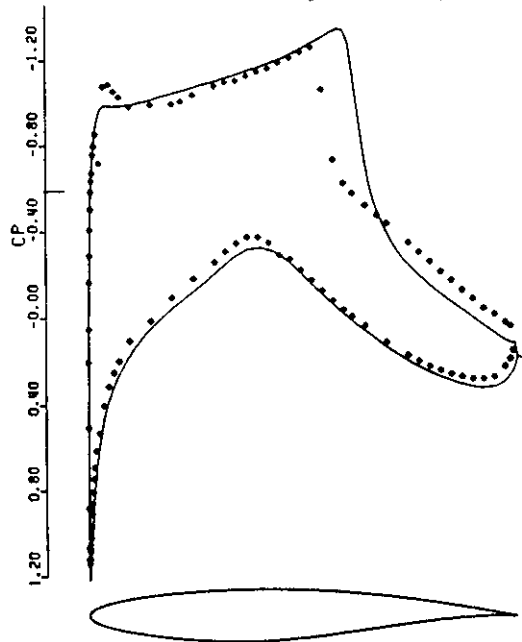
RAE2822 W-CYCLE TVD * 6
MACH 0.725 ALPHA 2.400
CL 0.7364 CD 0.0146 CM -0.0944
GRID 256X32 NCYC 75 RES0.136E-01

Fig. 8.3a
RAE 2822 airfoil case (6)
Pressure coefficient along the surface.
(Flux Limited dissipation model)
Solid line - Computed solution
* - Experiments (Ref. 14)



RAE2822 W-CYCLE TVD * 9
MACH 0.730 ALPHA 2.790
CL 0.8134 CD 0.0203 CM -0.0993
GRID 256X32 NCYC 75 RES0.152E-01

Fig. 8.3b
RAE 2822 airfoil case (9)
Pressure coefficient along the surface.
(Flux Limited dissipation model)
Solid line - Computed solution
* - Experiments (Ref. 14)



RAE2822 W-CYCLE TVD * 10
MACH 0.750 ALPHA 2.810
CL 0.8208 CD 0.0313 CM -0.1182
GRID 256X32 NCYC 75 RES0.990E-02

Fig. 8.3c
RAE 2822 airfoil case (10)
Pressure coefficient along the surface.
(Flux Limited dissipation model)
Solid line - Computed solution
* - Experiments (Ref. 14)